Reactivation of catalysts for methanol-to-hydrocarbons conversion with hydrogen

Vladimir Paunović [a,b,]*, Vitaly Sushkevich [b], Przemyslaw Rzepka [a,b], Luca Artiglia [b], Roland Hauert [c], Sung Sik Lee [d], Jeroen A. van Bokhoven [a,b,]*

[a] Institute for Chemical and Bioengineering, ETH Zurich, Vladimir-Prelog-Weg 1, 8093 Zurich, Switzerland
[b] Laboratory for Catalysis and Sustainable Chemistry, Paul Scherrer Institute, 5232 Villigen PSI, Switzerland
[c] Swiss Federal Laboratories for Materials Science and Technology, EMPA, Überlandstrasse 129, 8600 Dübendorf, Switzerland
[d] Scientific Center of Optical and Electron Microscopy, ETH Zurich, Otto-Stern-Weg 3, 8093 Zurich, Switzerland

ARTICLE INFO

ABSTRACT

Catalyst coking is one of the key challenges in hydrocarbons processing. Herein, we studied the potential of reacting coke deposits with hydrogen to regenerate the methanol–to–hydrocarbons (MTH) performance of archetypical ZSM-5 catalysts exhibiting low-to-medium Si/Al atomic ratios (14–39). The reactivation with hydrogen is substantially enhanced at elevated pressures (20–30 bar), restoring significant part of the MTH activity (>85%) and turnover capacity (>30%) at 753–823 K. Decoking is particularly efficient for the aluminum-rich catalyst, removing up to 96% of coke and attaining the performance comparable to conventional coke combustion. X-ray diffraction, Raman, infrared, nuclear magnetic resonance, and X-ray photoelectron spectroscopic analyses revealed that hydrogen eliminates internal and external coke from the catalyst with low Si/Al ratio, and internal coke from the silicon-richer materials. Hydrogen treatments yield light hydrocarbons (e.g., methane and ethane) and aromatics (e.g., methylated benzenes) offering thus a route for valorizing coke that can be exploited in other processes.

1. Introduction

Methanol (CH_3OH)-to-hydrocarbons (MTH) conversion over microporous solid acid catalysts is an integral step in the production of liquid fuels and essential petrochemicals from resources alternative to oil, such as methane (CH_4), carbon dioxide (CO_2), and hydrogen (H_2) [1–3]. The MTH transformation proceeds via an autocatalytic mechanism in which acid sites within the micropore confinement catalyze a series of methylation, cyclization, hydrogen transfer, and cracking reactions of the alkene- and arene-based hydrocarbon pool intermediates [1,3–5]. In addition to the desired lower-molecular weight products, such as alkenes, alkanes, and aromatics, that diffuse through the micropores, the MTH reaction inevitably yields (poly)alkylated polycyclic aromatic hydrocarbons (PAHs) that exhibit impaired diffusion and strong adsorption [6–9]. Consequently, PAHs occlude the micropores and cover the external crystal surface, forming thus internal and external coke, respectively. This results in catalyst deactivation due to blocked active sites and hampered mass transport of reactants and products. The rate of coke deactivation can be lowered by choosing the appropriate micropore topology, by tailoring the acid site concentration, crystallite size, Si/Al ratio, reaction conditions, or by doping [10–18]. Still, the maximum throughput capacities of MTH catalysts, including commercially-applied ZSM-5 and SAPO-34 are still limited up to ca. 1000–4000 g_{CH3OH} g_{cat}^{-1}. Considering the 10 to 100 times higher price of catalyst with respect to methanol, regeneration of their activity by coke combustion with diluted oxygen (O_2) or air at high temperature (773–873 K) constitutes an important part of commercial MTH processes [19–21]. Nonetheless, coke oxidation dissipates PAHs into carbon dioxide and steam, whereby the interaction of the latter product with the zeolite framework may result in an irreversible loss of structure and active sites, particularly in the hot-spots provoked by the high reaction exothermicity and impaired heat transfer [19,20]. On the other hand, coke combustion with more reactive oxidants, such as ozone (O_3) and nitrogen dioxide (NO_2), which can reduce the oxidizing temperature, or its oxidation with steam and CO_2 into CO exhibit limited potential due to challenging oxidant handling

* Corresponding authors at: Institute for Chemical and Bioengineering, ETH Zurich, Vladimir-Prelog-Weg 1, 8093 Zurich, Switzerland.
E-mail addresses: vladimir.paunovic@chem.ethz.ch (V. Paunović), jeroen.vanbokhoven@chem.ethz.ch (J.A. van Bokhoven).

(*e.g.*, O₃-enriched air), catalyst degradation (*e.g.*, NO₂ and steam), and unfavorable reaction thermodynamics (*e.g.*, CO₂ and steam) [19–21].

Reductive decomposition of coke with hydrogen represents an interesting concept of catalyst reactivation, which enables PAHs transformation into potentially useful hydrocarbons and minimizes the risk of steam-induced degradation [20,22]. Bauer *et al.*, showed that hydrogen treatment of the deactivated ZSM-5 catalysts at 773 K and 1 bar partially recovers their MTH activity [23]. Lee and Choi reported that exposure of coked ZSM-5 catalysts to hydrogen flow at 973 K and 1 bar eliminates up to 54% of coke and completely restores methanol conversion [9]. Zhao *et al.*, observed 40% coke loss after the reaction of deactivated SAPO-34 catalyst with hydrogen at 723 K and 5 bar [12]. In addition, Arora *et al.*, and Zhao *et al.*, revealed that co-feeding of hydrogen with methanol at elevated pressures (5–40 bar) impedes coking and markedly extends the throughput capacity of several MTH catalysts [11,12]. The reaction of hydrogen with coke and its precursors is rationalized by the ability of Brønsted acid sites (BAS) to catalyze the hydrogenation of the C=C bonds, with activity decreasing in the order dienes > alkenes > arenes [24]. These reactions proceed *via* a pathway that is the reverse reaction of alkane dehydrogenation. It encompasses the formation of intermediate penta-coordinated carbonium ion in the rate-limiting step, as supported by the first order dependence of their rates on the concentrations of hydrogen and hydrocarbons, the absence of H_2/D_2 kinetic effect, and theoretical studies [24–26]. Accompanied by skeletal isomerization, cracking, and disproportionation reactions, hydrogenation enables to decompose PAHs into lighter hydrocarbons that can be swept from zeolites [9,12,20,22,24]. The existing work suggests that hydrogen decomposes the internal coke, which is primarily composed of lighter PAHs (up to pyrene), yielding C_{1-3} alkanes [9,12,23]. Still, it provides no information on the potential evolution of C_{3+} hydrocarbons. In addition, the impact of the regeneration conditions, Brønsted acidity, and the extent of catalyst reactivation on the degree of coke removal and efficiency of reactivation are unknown.

Herein, we systematically studied the reactivation potential of hydrogen using prototypical ZSM-5 catalysts with varying acid properties that were deactivated under representative MTH conditions. Regeneration tests performed under different reaction conditions along with an in-depth characterization of the catalysts demonstrated that the coke decomposition and performance recovery with hydrogen feed can be substantially enhanced at moderate temperature by operating the reaction at elevated pressures. The performance regeneration is particularly efficient for catalysts with low Si/Al ratios, whereby it approaches the effectiveness of conventional coke combustion processes. We finally show that in addition to the light hydrocarbons, the coke decomposition under reductive hydrogen environment leads to the formation of heavier products such as alkylated benzenes and naphthalenes, which may open an interesting prospective for the revalorization of the coke deposits.

2. Experimental section

2.1. Catalysts

ZSM-5 catalysts with nominal Si/Al atomic ratios of 15 (CBV 3024E), 25 (CBV 5524G), and 40 (CBV 8014), which are denoted as Z_{15}, Z_{25}, and Z_{40} were obtained in ammonium form from Zeolyst International. They were transformed into protonic form by calcination under flowing air (500 cm³ STP min⁻¹) at 823 K for 5 h, using a heating rate of 5 K min⁻¹.

2.2. Catalyst characterization

The silicon and aluminum content of ZSM-5 catalysts was analyzed by inductively coupled plasma-optical emission spectroscopy (ICP-OES) using a Horiba Ultima 2 instrument equipped with a photomultiplier tube detector. The powder X-ray diffraction (XRD) patterns were collected at Bragg-Brentano geometry in a Bruker D8 ADVANCE diffractometer using Cu Kα radiation (λ = 1. 54 Å) generated by 2.2 kW Cu anode, which was operated at V = 40 kV and I = 20 mA. The data was recorded in the 2θ range of 5–70°, using a step size of 0.014° and acquisition time of 1.6 s per step. The lattice parameters of different samples were determined by refining their Bragg reflections in the space group *Pnma* using Pawley method and TOPAS 6 software [27]. Herein, the same instrumental function (except specimen displacements) was simultaneously refined against all collected X-ray diffractograms and the peak shape was fitted with pseudo-Voight function. N_2 isotherms were recorded at 77 K using a Micromeritics 3D Flex automatic surface area and pore-size analyzer. Prior to the analysis, the samples were evacuated at 673 K for 12 h. Coke content of the used catalysts was determined by thermogravimetric analysis (TGA) using NETZSCH STA 449 Jupiter analyzer. The samples (*ca.* 12 mg) were dried for 30 min at 573 K under flowing He (40 cm³ STP min⁻¹) and thereafter heated under flowing air (40 cm³ STP min⁻¹) up to 1173 K, using a heating rate of 10 K min⁻¹. Fourier transform infrared spectroscopy (FTIR) measurements were performed on a Thermo Scientific iS50 spectrometer equipped with a DTGS detector. The sample (*ca.* 20 mg) was pressed in a self-supported disc (area *ca.* 2 cm²) that was then placed in a quartz FTIR cell and degassed at 723 K for 3 h. After cooling down to room temperature, the FTIR spectra of the fresh and coked zeolites were collected in the range 650–4000 cm⁻¹ by accumulating 128 scans with a nominal resolution of 4 cm⁻¹. Pyridine adsorption was then performed by contacting the sample with 4 mbar of its vapors, which is followed by the cell evacuation at 423 K (*ca.* 0.6 h) to desorb the weakly adsorbed molecules. Thereafter, the cell was cooled down to room temperature to collect the spectrum. The final spectra were normalized to the sample's weight and processed using OMNIC 9.3 software. The concentrations of BAS and Lewis acid sites (LAS) were evaluated from the areas of the peaks centered at 1545 cm⁻¹ and 1454 cm⁻¹, respectively, using the molar integral excitation coefficients of ε_{BAS} = 1.67 cm μmol⁻¹ and ε_{LAS} = 2.94 cm μmol⁻¹ [28]. ²⁷Al and ¹H→¹³C cross-polarization magic angle spinning nuclear magnetic resonance (²⁷Al MAS NMR and ¹³C CP/MAS NMR) spectra were recorded using a Bruker Avance IIIHD 400 spectrometer equipped with a 9.4 T magnet. ²⁷Al MAS NMR spectra were recorded by using 2.5 mm ZrO₂ rotors that were spun at 10 kHz at a resonance frequency of 104.3 MHz. A single-pulse excitation with a recycle delay of 0.5 s, a sweep width of 400 ppm, and 4096 (Z_{15}) or 8192 (Z_{40}) accumulations were applied. ¹³C CP/MAS NMR spectra were collected by using 4 mm ZrO₂ rotors that were spun at 10 kHz at a resonance frequency of 75.5 MHz. The NMR spectra were normalized with respect to the sample weight. ²⁷Al triple- quantum (3Q) MAS NMR spectra were acquired on a Bruker Avance III HD 700 spectrometer equipped with a 16.4 T magnet. The spectra were measured by using a 2.5 mm ZrO₂ rotors that were spun at 20 kHz at a resonance frequency of 182.4 MHz. The double frequency swept had a duration of 12.5 μs and was swept from 50 to 800 kHz. The selective π pulse had a duration of 38 μs. Per the t_1 increment, 3456 scans with a recycle delay of 0.6 s were accumulated for a total of 32 increments over a spectral range of 548–219 ppm in the direct and indirect dimensions, respectively. Raman spectra were obtained by using a Horiba Lab-RAM HR Evolution instrument in a configuration that exploits 325 nm laser (source power 25 mW), 1800 mm⁻¹ grating, 40× objective lens (Thorlabs LMU-40X UVB), edge and holographic

notch filters, and Horiba Synapse CCD detector. The samples were prepared in the form of self-supported discs as described for FTIR and the spectra were acquired in the Raman shift range of 300–1700 cm^{-1} with 30 s acquisition time. The absence of laser-induced sample damage was ensured by visual inspection. Confocal fluorescence microspectroscopy of particles was performed using a Visitron spinning disk system equipped with inverted microscope (Nikon Eclipse TiE), EM-CCD camera (Andor iXon Ultra, Andor), a 100x objective lens (Nikon CFI Plan Apo), and appropriate excitation and emission detection filters. The signals associated with benzenic (B_n), naphthalenic (N_n), phenanthrenic (PH_n), and pyrenic (PY_n) species were recorded at the excitation wavelengths of 405, 488, 561, 640 nm and emission wavelengths of 450, 525, 605, 700 nm, respectively, and their profiles along the particles were extracted by Fiji software [29,30]. X-ray photoelectron spectroscopy (XPS) analysis was carried on a Physical Electronics Quantera X-ray photoelectron spectrometer using monochromatic Al Kα radiation that is generated from an electron beam operated at 15 kV, and equipped with a hemispherical capacitor electron-energy analyzer. The solids were analyzed at an electron takeoff angle of 45° and a pass energy of 55 eV. Thereby, electron and an ion neutralizer were operated simultaneously to minimize the sample charging. Silicon and carbon concentrations were quantified from the Si 2p and C 1s photoelectron peak integrals obtained after Shirley background subtraction using PHI-MultiPak software and the built-in relative sensitivity factors that are corrected for the system transmission function. Depth profiling of the samples was performed at the X07DB In Situ Spectroscopy beamline, Swiss Light Source, Villigen, Switzerland [31,32]. The zeolite samples were pressed with tantalum mesh into thin pellets, mounted on a manipulator and introduced into the solid-gas interface endstation. Photoemission spectra were acquired at 298 K by using linearly-polarized light and three different excitation energies for Si 2p (415, 720, and 920 eV), Al 2p (390, 690, and 890 eV), and C 1s (390, 690, and 890 eV) to generate the photoelectrons with kinetic energies of *ca.* 300, 600, and 800 eV. The pass energy of 50 eV was used for all the elements. The charging was minimized by feeding a nitrogen flow (10 cm^3 STP min^{-1}) over the pellet, which stabilized the pressure at 1 mbar. The C/Si and Si/Al molar ratios were calculated from the corresponding peak areas obtained after subtraction of Shirley background, which were normalized to the total number of scans, the beam photocurrent, the fraction of first order radiation, and the total photoionization cross sections at respective energy. The inelastic mean free path (IMFP) of the photoelectrons was calculated using the NIST Electron Inelastic-Mean-Free-Path Database, whereby Gries equation and assumption that properties of zeolites correspond to those of SiO$_2$ (1 g cm^{-3}) were adopted [33].

2.3. Catalytic testing

Catalytic and regeneration tests were performed in a home-made continuous flow fixed-bed reactor set-up. Gases, helium (He, PanGas, 5.0), hydrogen (PanGas, 5.0), oxygen (PanGas, 5.0), and ethene (PanGas, 20 mol% in He), were fed by set of gas modules (ThalesNano), and methanol (Fisher Scientific, 99.8%) and deionized water were fed by a syringe pump (CHEMYX Fusion 6000) and evaporated in helium stream by a thermostated mixer-vaporizer system. Catalysts (catalyst weight, W_{cat} = 50–80 mg, particle size, d_p = 0.18–0.25 mm) were mixed with silicon carbide (SiC, d_p = 0.3–0.4 mm, prewashed in nitric acid, and calcined) in a volume ratio of V_{cat}/V_{SiC} = 1/8 and loaded into a stainless steel reactor (internal diameter, d_i = 5 mm) between two plugs of quartz wool. The reactor was heated with an electric oven (CARBOLITE MTF 10/15). The reaction temperature was monitored by a K-type thermocouple that was placed in the middle of the catalyst bed, and

the reaction pressure was measured by using the pressure transducer (Keller) positioned prior to the reactor. All the linings exposed to methanol and hydrocarbons feeds were maintained at 453 K to preclude condensation. Prior to the MTH tests, the catalyst bed was heated in helium flow (300 cm^3 STP min^{-1}) at 723 K for 0.5 h, and then cooled down to the desired starting temperature. (heating/cooling rate of 10 K min^{-1}). Methanol feed was pre-stabilized through a bypass line and thereafter admitted to a reactor. MTH reactions were performed at 673 K and 1.5 bar using the inlet methanol flow of 0.08 cm$^3_{(lq)}$ min^{-1} (45 cm^3 STP min^{-1}) and helium flow of 190 cm^3 STP min^{-1}, which corresponds to a methanol concentration of 19 mol% and weight-hourly space velocities in the range of $WHSV$ = 47.5–76 g_{CH_3OH} g_{cat}^{-1} h^{-1}. After attaining a specific degree of catalyst deactivation, the reaction was terminated by replacing the methanol feed with helium (300 cm^3 STP min^{-1}), purging helium for 0.5 h, and then heating up to a temperature required for the hydrogen treatments or coke combustion, at which it was stabilized for 0.5 h. Prior to the treatment, the reactor was shortly purged with hydrogen and then pressurized with this gas by switching the flow through the pressure-regulating valve (Swagelok). Unless stated otherwise, hydrogen treatments were carried out by using a hydrogen flow of 100 cm^3 STP min^{-1} ($WHSV$ = 6.6–10.5 g_{H_2} g_{cat}^{-1} h^{-1}) at 753 or 823 K and 20 bar for 0.85–5 h. Coke combustion was performed by feeding 100 cm^3 STP min^{-1} of oxygen ($WHSV$ = 105 g_{O_2} g_{cat}^{-1} h^{-1}) over a catalyst at 823 or 873 K and 1.5 bar for 1.75 or 5 h.

The inlet and outlet reactor feeds were analyzed by (*i*) a mass spectrometer (MS, Pfeiffer Omnistar GSD 300 O2) to online monitor the content of methanol (m/z = 31), dimethyl ether (DME, m/z = 46), and helium (m/z = 4) in MTH tests, and to trace the evolution of light gases during hydrogen treatments, (*ii*) a gas chromatograph (Agilent GC 6890) equipped with a 6-port-2-position valve, a HP PLOT-Q column, and a flame ionization detector (FID) to online quantify methanol, DME, and hydrocarbons in the MTH tests, and to determine the gaseous products that were collected in a gas sampling bag during hydrogen treatments, and (*iii*) a GC (Agilent 7890A) equipped with an HP-5MS column and a MS detector (Agilent 5975C XL MSD) to determine the aromatic products that were collected in a cold trap (273 K) containing dichloromethane (internal standard/ tetrachloroethene, C$_2$Cl$_4$) during hydrogen treatments.

Conversion (X), selectivity to hydrocarbon product C$_x$H$_y$ ($S_{C_xH_y}$), and methanol cumulative turnover capacity (CT) were calculated according to Eqs. 1–3, respectively, in which $\dot{n}_{i,\,in}$ and $\dot{n}_{i,\,out}$ denote the inlet and outlet molar flows of species i, respectively, and x denotes the number of carbon atoms in hydrocarbon product C$_x$H$_y$. The carbon balance was higher than 96% in all experiments.

$$X = \frac{\dot{n}_{CH_3OH,\,in} - (\dot{n}_{CH_3OH,\,out} + 2 \times \dot{n}_{DME,\,out})}{\dot{n}_{CH_3OH,\,in}},\ \% \tag{1}$$

$$S_{C_xH_y} = \frac{x \times \dot{n}_{C_xH_y,\,out}}{\sum x \times \dot{n}_{C_xH_y,\,out}},\ \% \tag{2}$$

$$CT = WHSV \int_0^t X dt,\ g_{CH_3OH}\ g_{cat}^{-1} \tag{3}$$

3. Results and discussion

3.1. Performance recovery

The assessment of the hydrogen potential to restore the activity of the coked MTH catalysts was commenced by analyzing the MTH deactivation and hydrogen reactivation of the Z$_{15}$ material, which

is an archetypical aluminum-rich ZSM-5 zeolite (Si/Al atomic ratio of 14 as determined by ICP-OES) with high propensity to coking (Fig. 1a) [34]. Catalyst deactivation was studied under the conditions of incomplete initial conversion (*ca.* 92%) to determine the activity changes during the MTH-regeneration cycles and to ensure that coking contributions of both reactants and products are displayed across a complete catalyst bed. Herein, the MTH reaction was quenched at low ($X \approx 80\%$), medium ($X \approx 56\%$), and high ($X \approx 30\%$) deactivation points, and corresponding $Z_{15}M_l$, $Z_{15}M_m$, and $Z_{15}M_h$ catalysts were subsequently exposed to a hydrogen flow. The starting temperature (753 K) and duration (1.75 h) of the hydrogen treatments were selected based on criteria that their values should not differ significantly from the operating temperatures and time spans of the MTH reaction and conventional coke oxidation in order to minimize the thermal degradation of the catalyst. However, as exemplified with $Z_{15}M_m$ catalyst, hydrogen treatment under these conditions and applying a pressure of 6 bar did not yield any significant reactivation in thus obtained $Z_{15}M_mH$ material. This is consistent with the study of Lee and Choi who showed that in the lower pressure ranges temperatures as high as 973 K are required for hydrogen-induced decoking of ZSM-5 catalysts deactivated in MTH conversion [9]. The positive impact of elevated hydrogen pressures on the hydrogenation activity of zeolites and on the catalyst stability in MTH reaction led us to investigate the impact of elevated hydrogen pressures on the reactivation of $Z_{15}M_m$ [24,35]. Herein, the treatment performed at 20 bar yielded a substantial catalyst reactivation (Fig. 1a). In particular, the resulting $Z_{15}M_mH_m$ catalyst exhibited an initial conversion of 82%, while its cumulative turnover until reaching the point of medium conversion decay corresponds to *ca.* 54% of the fresh Z_{15} catalyst. A control experiment performed by exposing the $Z_{15}M_m$ catalyst to

a helium flow at 20 bar and 753 K while maintaining other conditions identical to hydrogen treatment yielded $Z_{15}M_mHe$ catalyst that did not induce any significant recovery of activity. This indicates that reactivation effect of hydrogen stems from its chemical reaction with coke. Comparatively, $Z_{15}M_lH_m$ and $Z_{15}M_hH_m$ materials obtained after the exposure of mildly and highly deactivated catalysts to high-pressure hydrogen feed displayed the initial conversions that are similar to and slightly (*ca.* 10%) lower, respectively, with regard to the fresh Z_{15} catalysts. The product distribution of all reactivated catalysts showed no significant deviations from that of the parent Z_{15} zeolite (Fig. S1). In turn, the ratio of the CT capacities of the reactivated and fresh catalysts until attaining an identical level of conversion at which reactivation was performed, $CT_{X,r}/CT_{X,f}$, are in the range of 0.5–0.6 (Fig. 1b). The experiment in which $Z_{15}M_l$ catalyst is exposed to several deactivation-reactivation cycles shows that the reactivation effect of hydrogen treatments extends beyond a single regeneration (Fig. 1a). Thereby the $CT_{X,r}/CT_{X,f}$ ratio of the respective $Z_{15}M_cH_c$ catalyst after the last reactivation step is slightly (*ca.* 15%) lower with respect to $Z_{15}M_lH_m$ material (Fig. 1b).

The recovery of the CT capacities is also accessed by varying the time span and temperature of the high-pressure hydrogen treatments performed over the representative $Z_{15}M_m$ catalyst. Increase of treatment time from 0.85 h ($Z_{15}M_mH_l$) to 5 h ($Z_{15}M_mH_h$) as well as a moderate increase of temperature from 753 K to 823 K ($Z_{15}M_mH_T$) resulted in substantial enhancement of the cumulative turnovers and moderate increase of the initial activity (Fig. 1). Notably, the initial activities and $CT_{X,r}/CT_{X,f}$ values of $Z_{15}M_mH_h$ and $Z_{15}M_mH_T$ materials were approaching those displayed by the reference $Z_{15}M_mO$ catalyst obtained after the combustion of coke deposits from $Z_{15}M_m$ at 823 K and 1.5 bar for 1.75 h. This result
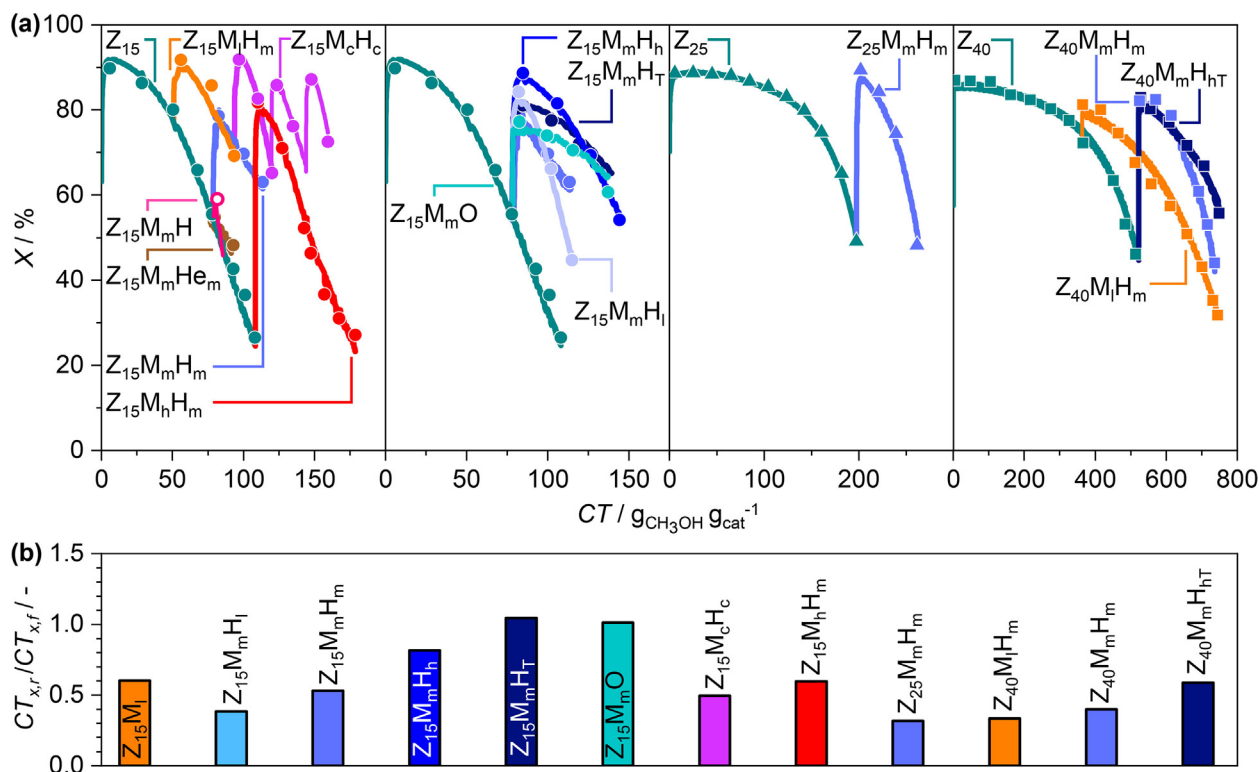
Fig. 1. (a) MTH deactivation profiles and (b) corresponding $CT_{X,r}/CT_{X,f}$ values of Z_{15}-, Z_{25}-, and Z_{40}-based catalysts in fresh form and after reactivation with hydrogen, oxygen, or helium. Markers and lines in (a) indicate conversion calculated from GC-FID and MS analysis, respectively. Conditions: MTH: T = 673 K, P = 1.5 bar, c_{CH_3OH} = 19 mol%, and $WHSV$ = 47.5 (Z_{40}-based samples), 63 (Z_{25}-based catalysts), or 76 g_{CH_3OH} g_{cat}^{-1} h^{-1} (Z_{15}-based catalysts). Hydrogen reactivation: T = 753 or 823 K, P = 6 ($Z_{15}M_mH$) or 20 bar (other samples), c_{H_2} = 100 mol%, $WHSV$ = 6.6 (Z_{40}–based catalysts), 8.8 (Z_{25}–based catalysts), or 10.5 g_{H_2} g_{cat}^{-1} h^{-1} (Z_{15}–based catalysts), and *tos* = 0.85–5 h. Oxygen reactivation: T = 823 K, P = 1.5 bar, c_{O_2} = 100 mol%, $WHSV$ = 105 g_{O_2} g_{cat}^{-1} h^{-1}, and *tos* = 1.75 h. Helium reactivation: T = 753 K, P = 20 bar, c_{He} = 100 mol%, $WHSV$ = 21 g_{He} g_{cat}^{-1} h^{-1}, and *tos* = 1.75 h.

indicates an interesting potential of the high-pressure hydrogen treatments in reactivating the MTH catalysts at moderate temperatures. Therein, the initial conversion and $CT_{X,r}/CT_{X,f}$ ratio of $Z_{15}M_mO$ catalyst were also lower than those of fresh Z_{15} material, although the former material is almost free from coke deposits (*vide infra*).

To assess the impact of the aluminum content of a catalyst on the extent of performance regeneration by hydrogen, the reactivation with high-pressure hydrogen feed was also studied over Z_{25} and Z_{40} catalysts, which have Si/Al atomic ratios of 23 and 39, respectively, as determined by ICP-OES. The MTH reaction was performed under the same conditions that were applied for the Z_{15} material, except that the *WHSV* was reduced to ensure comparable initial conversion for three catalytic systems. The reaction was quenched after attaining medium extent of deactivation ($X \approx$ 52%) and both catalysts were then subjected to hydrogen feed at 753 K and 20 bar for 1.75 h. The initial activity of thus obtained $Z_{25}M_mH_m$ ($X \approx 89\%$) and $Z_{40}M_mH_m$ ($X \approx 86\%$) catalysts was recovered to a higher extent in comparison to $Z_{15}M_mH_m$ ($X \approx 80\%$), while their product distribution profile was essentially unaltered with respect to corresponding Z_{25} and Z_{40} catalysts (Fig. 1a, Fig. S1). However, their $CT_{X,r}/CT_{X,f}$ ratios were lower than for $Z_{15}M_mH_m$ (Fig. 1b). Similarly, hydrogen treatment of mildly deactivated $Z_{40}M_l$ catalyst led to a lower (*ca.* 32%) recovery of CT_X capacity than for $Z_{15}M_lH_m$. In view of previously established effects of treatment time and temperature on the recovery of CT_X capacities, the representative $Z_{40}M_m$ material was exposed to hydrogen feed at increased temperature (823 K) and for longer time (5 h). The resulting $Z_{40}M_mH_{hT}$ catalyst displayed an increase of the $CT_{X,r}/CT_{X,f}$ ratio (*ca.* 40%) with respect to $Z_{40}M_mH_m$ (Fig. 1).

3.2. Coke content, micropore volume, and acidity recovery

Consistent with the observed MTH performance trends (Fig. 1), the coke content of $Z_{15}M_m$ catalyst progressively decreased with extending the exposure time to high-pressure hydrogen feed as well as by increasing the temperature of the treatment (Fig. 2a). Therein, $Z_{15}M_mH_h$ and $Z_{15}M_mH_T$ materials displayed the most pronounced reduction of the coke content (*ca.* 76% and 85%, respectively), which is consistent with the highest degree of activity and *CT* recovery that is observed over these materials (Fig. 1). A treatment of $Z_{15}M_m$ catalyst with hydrogen at 753 K and 20 bar for 1.75 h in a glass vial that was placed inside the stainless steel reactor led to an almost identical removal of coke (*ca.* 72%) as recorded for the $Z_{15}M_mH_m$ catalyst (*ca.* 74%), thus ruling out the contribution of the stainless steel walls to decoking (Fig. S2). Comparatively, a decrease of the coke content over $Z_{25}M_mH_m$ (*ca.* 45%), $Z_{40}M_mH_m$ (*ca.* 35%), and $Z_{40}M_mH_{hT}$ (*ca.* 60%) with respect to the corresponding deactivated catalysts was lower than for respective Z_{15}-based materials. Decoking of the samples exposed to hydrogen feed is also reflected by the recovery of their micropore volumes (Fig. 2b). However, the values of these parameters were lower as compared to the parent zeolites, and in the case of hydrogen-reactivated $Z_{15}M_m$ catalysts slightly lower than for oxygen treated $Z_{15}M_mO$ sample. Similar to the fresh materials, the powder X-ray diffractograms of all hydrogen-treated samples exhibited well-resolved reflection doublets at $2\theta \approx 23.5$ and $45°$, which contrasts the broad reflections of the deactivated $Z_{15}M_m$, $Z_{25}M_m$, and $Z_{40}M_m$ catalysts (Fig. S3). The reflections at these 2θ angles are sensitive to the contraction of a and elongation of b unit cell parameters, which are induced by coke deposition [36]. The difference between a and b is a useful descriptor that primarily reflects the content of internal coke that is expected to have the prevailing contribution to the lattice microstrain. Calculation of a and b parameters by using Pawley method and determination of the corresponding a-b differences for fresh, deactivated, and reactivated samples reveals that

high-pressure hydrogen feed leads to a decrease of the lattice microstrain (Fig. 2c). Notably, $Z_{15}M_mH_h$ and $Z_{15}M_mH_T$ catalysts exhibit the a-b values that are comparable to the fresh and oxygen-treated materials, which suggests the efficient removal of internal coke. In comparison to $Z_{15}M_m$, $Z_{25}M_m$, and $Z_{40}M_m$ materials display smaller reduction of a-b parameter with respect to their fresh counterparts, which may imply lower fraction of internal coke in these samples.

In addition to the changes of the textural properties, catalyst deactivation in MTH reaction is also accompanied by a decrease in acid site concentration, which is caused by coke deposition and/or partial dealumination of the zeolite framework [9,37]. The intensities of the FTIR bands that are associated with O–H stretching of BAS and pyridine adsorption experiments indicate a moderate decrease of BAS in deactivated $Z_{15}M_m$ and $Z_{40}M_m$ catalysts with respect to fresh materials and no significant regeneration of the BAS even after prolonged hydrogen treatments (Fig. 3a, Fig. S4). Besides, BAS concentration in the oxygen-treated $Z_{15}M_mO$ sample is also comparable to that of the deactivated $Z_{15}M_m$. In line with these findings, ^{27}Al MAS NMR spectra of selected deactivated and reactivated Z_{15} and Z_{40} catalysts exhibit lower intensity of the resonance corresponding to the tetrahedral aluminum sites (T_d, *ca.* 55 ppm) in comparison to respective fresh samples, and its upfield broadening, while the resonant signal of the octahedral aluminum species (O_h, *ca.* 0 ppm) displays only a small increase. The incomplete recovery of BAS and T_d signal intensity in the ^{27}Al MAS NMR spectra can be rationalized by the existence of residual coke, which even if present in small amounts as it is the case for $Z_{15}M_mO$ catalyst (*vide infra*), can strongly interact with BAS and thus increase the quadrupole couplings by precluding the adsorption of water [21,38]. Such interaction results in weaker and broader T_d signals, with peak maxima shifted towards higher fields, whereby these changes correlate with coke content. In addition to the coke interaction with BAS, distortion or partial dissociation of the tetrahedral aluminum sites may also occur as a result of their interaction with byproduct steam, which is generated in substantial amounts under high *WHSV* applied in the MTH reaction tests [37,39]. To gain insights into the impact of steaming, additional experiments were performed (Fig. S5). In particular, $Z_{15}M_m$ catalyst was reactivated with oxygen at increased temperature (873 K *vs.* 823 K) for extended period of time (5 *vs.* 1.75 h). Characterization of thus obtained reactivated material, which is referred as $Z_{15}M_mO_{hT}$, by TGA and Raman analysis indicated a virtually complete removal of coke species. Consistent with this, the initial conversion in the MTH reaction over $Z_{15}M_mO_{hT}$ (*ca.* 88%) was higher than that over $Z_{15}M_mO$ (*ca.* 83%) catalyst, but still lower than that of Z_{15} material (*ca.* 92%). Notably, the intensity of T_d signal in the ^{27}Al MAS NMR spectra of $Z_{15}M_mO_{hT}$ catalyst was also lower in comparison to the parent Z_{15} catalyst. In addition, ^{27}Al triple-quantum (3Q) MAS NMR indicated small broadening of the signal in both F_1 and F_2 dimensions in $Z_{15}M_mO_{hT}$ with respect to parent Z_{15} catalyst, which points to a more prominent deterioration of the tetrahedral aluminum coordination in the latter sample (Fig. S4). The changes of the tetrahedral aluminum sites are also reflected by the lower activity of the $Z_{15}M_mO_{hT}$ with respect to Z_{15} catalyst in the methanol-to-DME dehydration, which is used as probe reaction sensitive to the concentration and strength of BAS [40]. To inspect the impact of water byproduct, Z_{15} was exposed to steam at conditions emulating the MTH conversion (Fig. S5). The resulting material, which is referred as $Z_{15}S$, exhibited a decrease of T_d signal intensity in the ^{27}Al MAS NMR spectrum as well as reduced activity in methanol-to-DME dehydration (Fig. S5). These complementary experiments corroborate the change of the aluminum tetrahedral sites during the MTH reaction, which mainly encompass distortion of their geometry or formation of partially dissociated framework-associated aluminum species, with absence
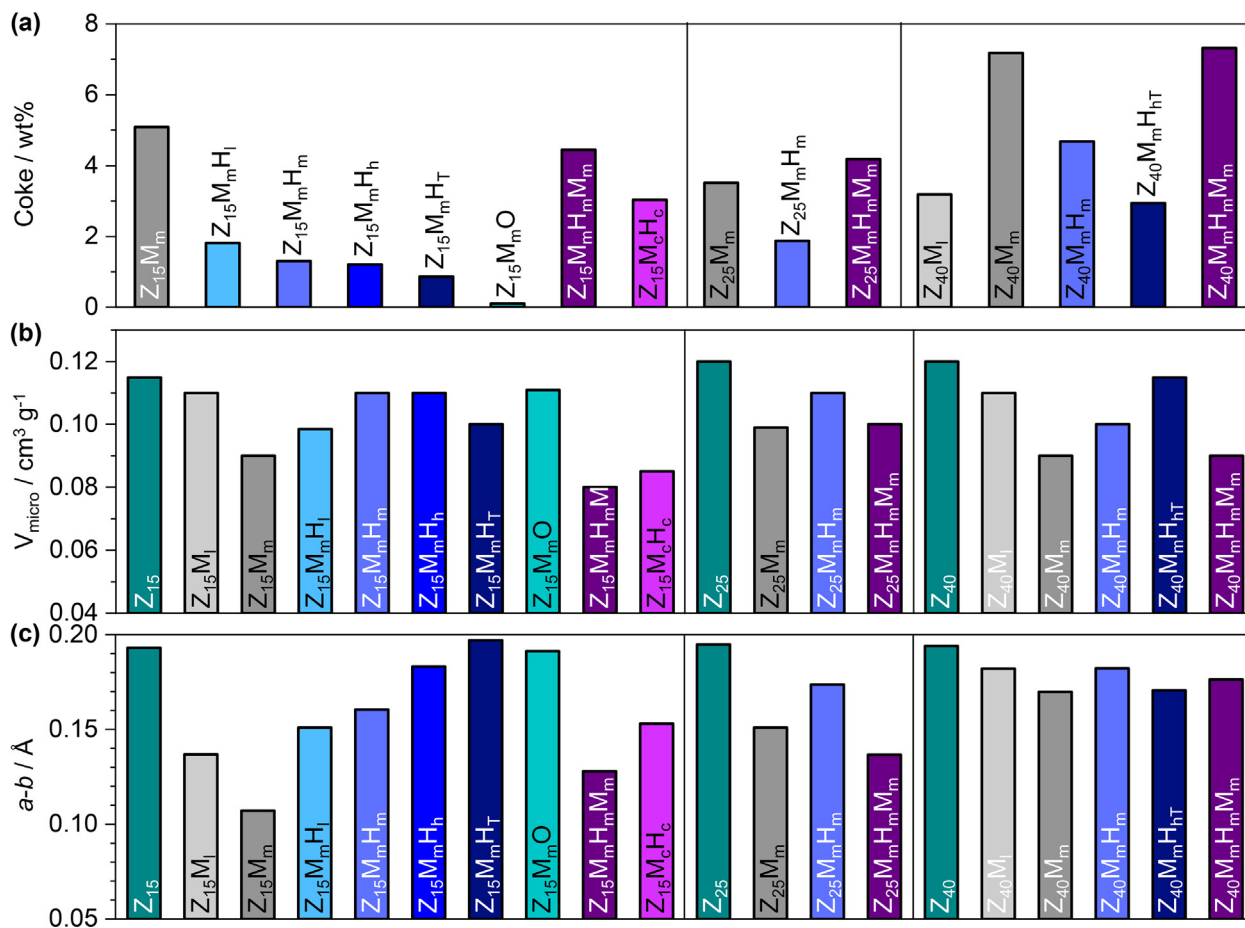
Fig. 2. (a) Coke content, (b) micropore volume, and (c) difference of *a* and *b* lattice parameters of selected Z_{15}-, Z_{25}-, and Z_{40}-based catalysts in fresh form, after deactivation in MTH reaction, and subsequent reactivation with hydrogen or oxygen. Conditions applied in MTH reaction and catalyst reactivation with hydrogen or oxygen correspond to those specified in the caption of Fig. 1.

of extensive aluminum dislodgment from the framework. Along with incomplete coke removal, these changes can also contribute to the incomplete recovery of the initial activity by the hydrogenation treatments.

3.3. Coke decomposition

Additional insights into the coke reaction with high-pressure hydrogen feed were acquired by analyzing the products evolving during the regeneration of the representative $Z_{15}M_m$ and $Z_{40}M_m$ catalysts (Fig. 4, Fig. S6). The online MS analysis of the effluent reactor stream revealed the prominent changes for the signals at *m*/*z* ratios of 16, 18, 31, 28, and 41 that can be associated with the generation of methane, water, methanol, C_2, and C_3 hydrocarbons (alkanes and alkenes), respectively. The evolution of C_1-C_3 hydrocarbons was also observed in the previous studies on hydrogen reaction with coked ZSM-5 and SAPO-34 zeolites at low pressures [9,12]. These molecules might be produced via dealkylation of PAHs (*vide infra*). The evolution of water and methanol in the early stages of the process might arise from several sources, including the reaction of the previously occluded methanol/metoxy species, release of the water that was occluded with coke, or as a result of decomposition of potentially present oxygen-contain coke species, the existence of which was discussed in the previous studies [6]. Herein, the amount of water evolving during the hydrogenation treatments of both catalysts was estimated to account for less than 6% of the decomposed coke, suggesting thus a small fraction
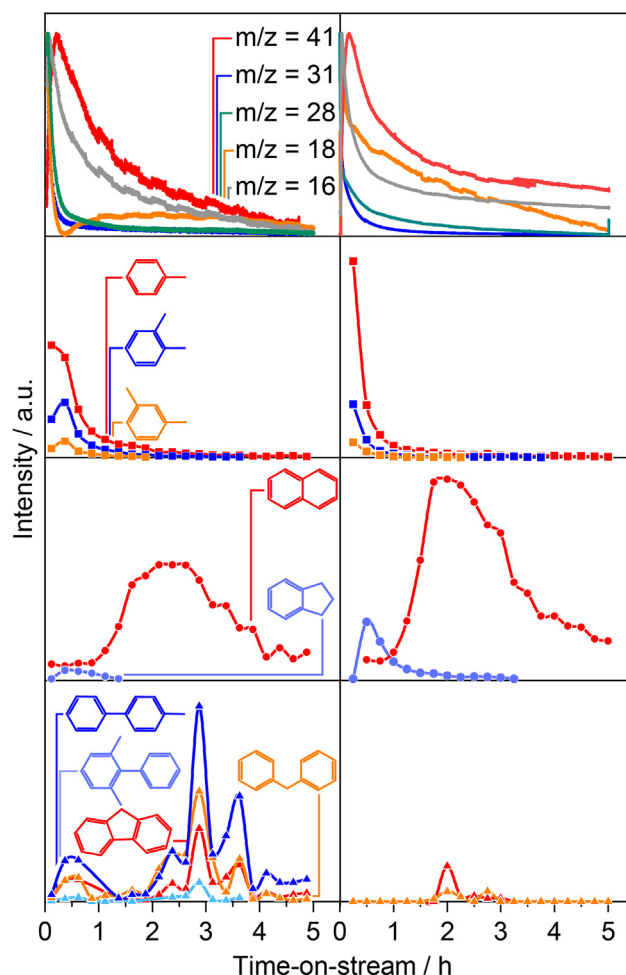
of oxygen-containing compounds (including residual water and methanol) in the deactivated catalysts. The GC–MS analysis of the products quenched in the dichloromethane cold trap during the hydrogenation treatment indicated the formation of more complex aromatics, including methylated benzenes, naphthalenes, biphenyls, and semihydrogenated compounds such as fluorene, which were not reported in previous works (Fig. 4, Fig. S6) [9,12]. Relative concentrations of these species were over five times higher compared to the experiment in which the catalyst was exposed to a high-pressure helium feed, indicating that their evolution is primarily associated with coke decomposition with hydrogen, and to a lower extent by their sweep from the catalyst pores (Fig. S6). Alkylated benzenes were the main products of the first reactivation phase, while higher molecular weight aromatics such as (alkylated) naphthalenes and biphenyl evolved during the later stages of reaction. These results, which are in line with the positive impact of the longer reactivation times on the recovery of the catalytic performance and coke elimination (Fig. 1), suggest slower decomposition of more condensed PAHs. Besides, they also indicate that hydrogen-induced transformation of PAHs into aromatic products can provide an interesting pathway for the valorization of coke.

To comprehend the product analysis, the changes in the coke composition upon hydrogen treatments were also studied. UV-Raman spectra of deactivated and hydrogen-reactivated samples display a prominent ring stretching mode of PAHs that is overlapped with graphitic carbon (G band, 1620 cm^{-1}), as well as the
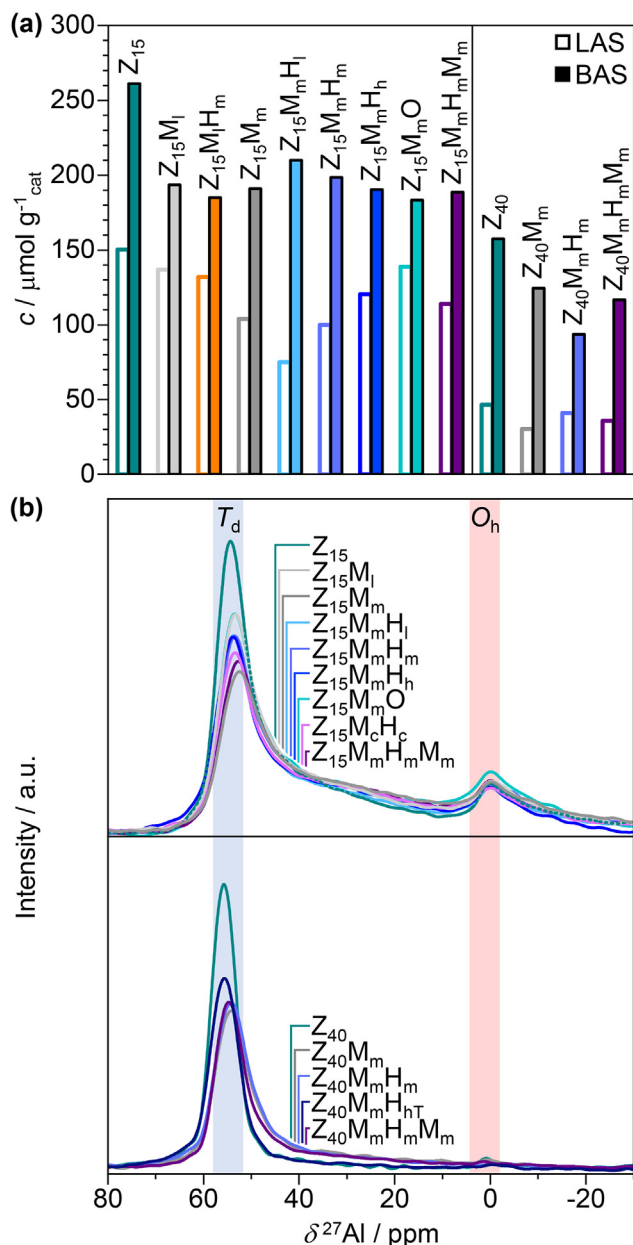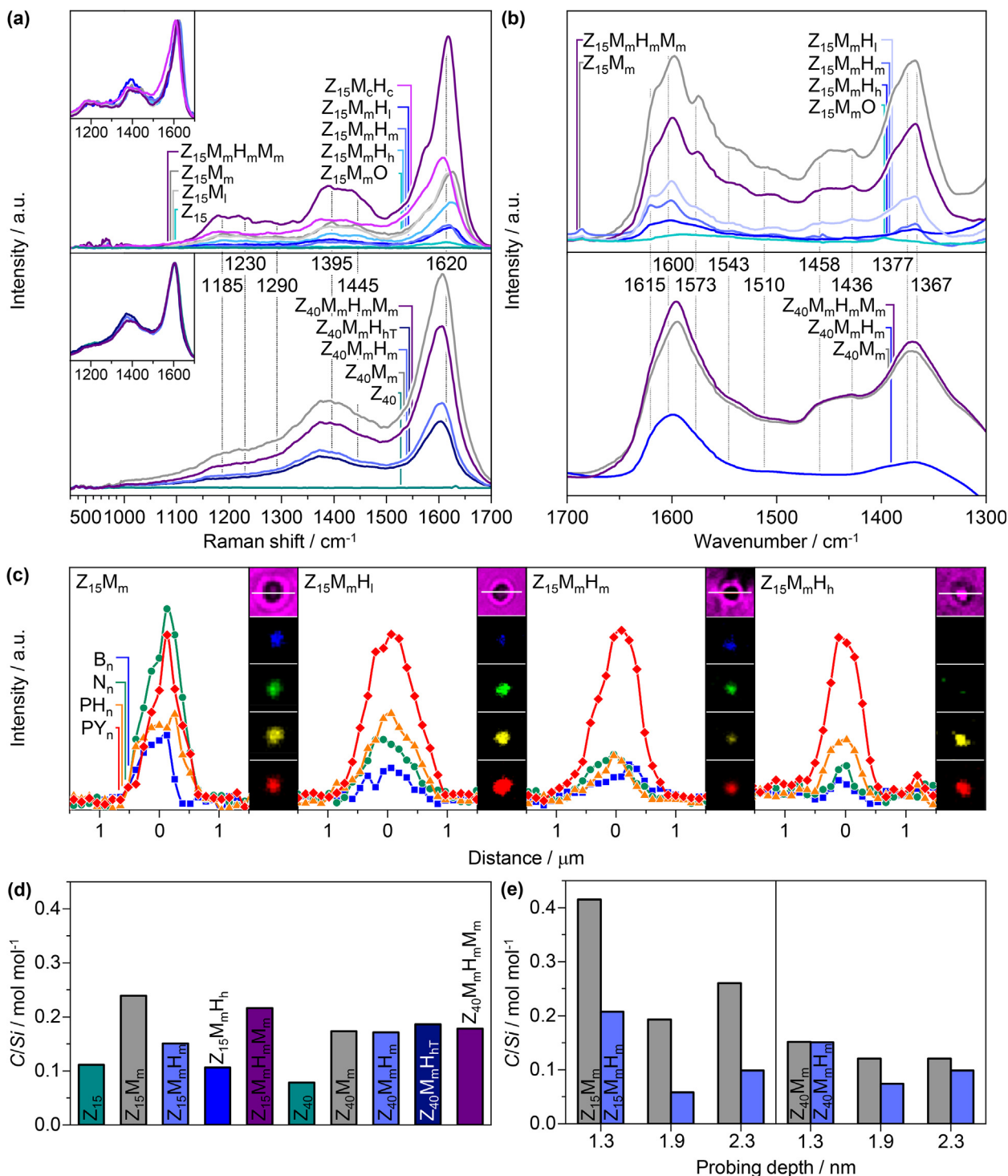
Fig. 3. (a) BAS and LAS concentrations and (b) ^{27}Al MAS NMR spectra of selected Z_{15}- and Z_{40}-based catalysts in fresh form, after deactivation in MTH reaction, and subsequent reactivation with hydrogen or oxygen. Conditions applied in MTH reaction and catalyst reactivation with hydrogen or oxygen correspond to those specified in the caption of Fig. 1.

Fig. 4. Evolution of various products during high-pressure hydrogen treatment of $Z_{15}M_m$ catalyst at T = 753 K (left) and $Z_{40}M_m$ catalyst at T = 823 K (right). Other conditions applied in catalyst reactivation with hydrogen correspond to those specified in the caption of Fig. 1.

ring stretches of long conjugated PAHs that compose a hard coke (D band, 1395 cm^{-1}, Fig. 5a, Fig. S7) [7,41–43]. Besides, the spectral features that are characteristic of lower molecular weight (1230 cm^{-1}), linearly condensed (1185 cm^{-1}), and alkylated/methylated (1185 cm^{-1}/1445 cm^{-1}) PAHs, as well as the vibrations of alkene C=C bonds (1290 cm^{-1}) are also observable. Although the resonance enhancement effects in the condensed aromatic compounds result in lack of the linear relationships between their content and Raman signal intensity, coke bands of deactivated catalysts display a decrease after the hydrogen treatment and an increase after the subsequent exposure to the MTH reaction [41]. The intensities of the coke spectral fingerprints decrease with increasing the treatment time and temperature. Still, they are higher as compared to the oxygen-treated sample, which still exhi-

bits G and D bands. In agreement with the differences in the reactivation behavior and extent of coke removal, the relative decline of the coke specific bands in $Z_{40}M_mH_m$ and particularly $Z_{25}M_mH_m$ with respect to $Z_{40}M_m$ and $Z_{25}M_m$ is lower than that in the case of hydrogen-treated $Z_{15}M_m$ catalyst. Normalization of the Raman spectra to the most intense G band reveals similar distribution of the spectral features in deactivated and hydrogen-reactivated samples, which suggests mostly uniform decomposition of coke during the exposure to high-pressure hydrogen feed (Fig. 5b, inset). The main exception to this trend is an increase in the relative fraction of D band in $Z_{15}M_mH_h$, $Z_{40}M_mH_m$, and $Z_{40}M_mH_{hT}$ catalysts, which suggests an increasing fraction of 'hard' coke. The FTIR spectra of the representative Z_{15}- and Z_{40}-based catalysts complement these findings (Fig. 5b). Herein, the bands originating from the C=C stretching in PAHs (1620–1575 and 1540–1510 cm^{-1}) and C-H bending modes in their alkyl substituents (1335–1410 and 1420–1470 cm^{-1}) show a prominent decrease after hydrogen reactivation [44–46]. Nonetheless, while the ratios of these bands are similar in deactivated and hydrogen-treated Z_{15} samples, alkyl bands decrease to a higher extent than the aromatic ring bands in the case $Z_{40}M_mH_m$ with respect to $Z_{40}M_m$ material. Likewise, ^{13}C CP/MAS NMR spectra indicate that the signals associated with aromatic rings (123–160 ppm) and aliphatic alkyl substituents (8–24 ppm) decrease after the hydrogen treatment of $Z_{15}M_m$ samples, whereas the reactivated $Z_{40}M_mH_m$ material preserves the

Fig. 5. (a) Raman spectra, (b) FTIR spectra, (c) confocal fluorescence microspectroscopy profiles, (d) surface content of carbon, and (e) surface depth-profile of carbon content of selected Z_{15}- and Z_{40}-based catalysts in fresh form, after deactivation in MTH reaction, and subsequent reactivation with hydrogen or oxygen. The Raman spectra in (a) are normalized with respect to the most prominent zeolite peak (*ca.* 381 cm^{-1}), while the insets display the spectra that are normalized with respect to the G band (*ca.* 1620 cm^{-1}). The signal profiles in (d) are derived along the lines indicated in confocal fluorescence micrographs, which are presented on the right of the respective panels. Conditions applied in MTH reaction and catalyst reactivation with hydrogen or oxygen correspond to those specified in the caption of Fig. 1.

intense aromatic resonances (Fig. S8) [47]. This implies that hydrogen treatments of the former catalyst lead to a mostly uniform decomposition of various PAHs, while in the latter catalyst they result in preferential dealkylation and/or decomposition of alkylated PAHs. Additional insights into the coke composition over $Z_{15}M_m$ and corresponding hydrogen treated catalysts were

obtained from confocal fluorescence microspectroscopy (Fig. 5c). Although the small size of the Z_{15} zeolite crystals (*ca.* 0.5–2 μm) precluded their detailed mapping, the confocal fluorescence microspectroscopy provided valuable information on the relative changes in the concentration profiles of methylated benzenic (B_n), naphthalenic (N_n), phenanthrenic (PH_n), and pyrenic (PY_n)

species [29]. The comparison of these profiles, which are normalized with respect to the intensity of the pyrenic signal, indicates that the decomposition of benzenic and napthalenic species proceeds relatively fast. The decomposition of more condensed phenanthrenic and pyrenic structures requires longer treatment times, which can be associated with their higher thermodynamic stability. In overall, the spectroscopic characterization indicate that hydrogen treatment of the $Z_{15}M_m$ catalyst leads to a decomposition of less and more condensed PAHs, *i.e.*, both 'hard' and 'soft' coke, respectively, while in the case of $Z_{40}M_m$ catalyst they preferentially remove 'soft coke'. These results are consistent with substantial relaxation of the unit cell parameters after the hydrogenation treatments and thus reduction of the lattice strain of all deactivated catalysts, which implies the elimination of 'internal' coke from the zeolite micropores (Fig. 2c). The latter is mostly composed of less condensed PAHs, *i.e.*, 'soft' coke. A higher extent of coke decomposition over $Z_{15}M_m$ in comparison to $Z_{40}M_m$ catalyst is also reflected in the photoemission spectra (Fig. 5d). Herein, the C/Si molar ratio in the surface region of the $Z_{15}M_mH_m$ displays a prominent decrease with respect to the deactivated $Z_{15}M_m$ catalyst. This contrasts an almost unchanged surface content of carbon in reactivated $Z_{40}M_mH_m$ and $Z_{40}M_mH_{hT}$ catalysts as compared to $Z_{40}M_m$. Depth-profile analysis of the carbon content over two representative sets of catalysts, $Z_{15}M_m$ and $Z_{15}M_mH_m$, and $Z_{40}M_m$ and $Z_{40}M_m$-H_m further corroborates these observations (Fig. 5e). In particular, the top-most region of $Z_{15}M_m$ catalysts (*ca.* 1.1 nm) displays an increased content of carbon, which after high-pressure hydrogen treatment decreases *ca.* 2 times. A decrease in carbon content is even more pronounced in the layers that are more distant from the surface (*ca.* 1.9 and 2.3 nm). Contrastingly, concentration of carbon at the most shallow probing depth (*ca.* 1.1 nm) is almost identical for the $Z_{40}M_m$ and $Z_{40}M_mH_m$ catalyst, and slightly decreased (<40%) in the deeper catalyst layers. The deconvolution of the C 1 *s* signals acquired at different probing depths indicates that component associated with C—C or C=C bonds in PAHs is mostly decreasing in the top-most region after treating the $Z_{15}M_m$ sample with hydrogen, which further suggests the decomposition of surface-confined coke (Fig. S9). In contrast, the relative

fraction of this component is almost unchanged after the exposure of $Z_{40}M_m$ sample to hydrogen. Notably, the XPS data evidence that high-pressure hydrogen feed can also decompose the external coke species over aluminum-rich catalysts, which contrasts the previous conclusions that these treatments primarily remove internal coke [9]. This also parallels the observation that 'hard' coke, which constitutes the main fraction of the surface carbonaceous deposits, is more efficiently decomposed over $Z_{15}M_m$ catalyst. Hereby, a depth-profile analysis of Si/Al atomic ratios over Z_{15}- and Z_{40}-based catalysts shows a surface enrichment in aluminum content with respect to the bulk (Fig. S10). More efficient coke removal by high-pressure hydrogen feed in the case of the catalysts with lower Si/Al ratios can be thus associated with higher surface aluminum content and hence the concentration of BAS that facilitate the decomposition of external coke. Still, the impact of different chemical structure of the surface confined PAHs species (*e.g.*, aromatic structures that have different degree of condensation) over the catalysts with different Si/Al ratios on the degree of external coke removal cannot be completely ruled out. At this point it also is noteworthy that the more pronounced decomposition of coke over the zeolite with higher BAS density may also contribute to the more pronounced enhancement of their cumulative turnover capacities in the presence of the high-pressure hydrogen co-feeds [11,12].

3.4. Enhancing the coke decomposition

Considering a high regeneration extent attained over the $Z_{15}M_m$ (Fig. 1 and 2), this sample was also exposed to an increased pressure of hydrogen of 30 bar at 823 K for 4 h in order to access if the decomposition of coke can be further promoted over this ZSM-5 material. The deactivation profile and the corresponding $CT_{X,r}/CT_{X,f}$ value of thus reactivated $Z_{15}M_mH_P$ closely match that of oxygen-treated $Z_{15}M_mO$ sample (Fig. 6a). Notably, the residual coke content of the $Z_{15}M_mH_P$ catalyst (*ca.* 0.2 wt%, Fig. 6b) decreased and the extent of coke removal (*ca.* 96%) increased in comparison to the $Z_{15}M_mH_T$ and $Z_{15}M_mH_h$ catalysts, attaining thus the levels that are comparable to those observed after the conven-
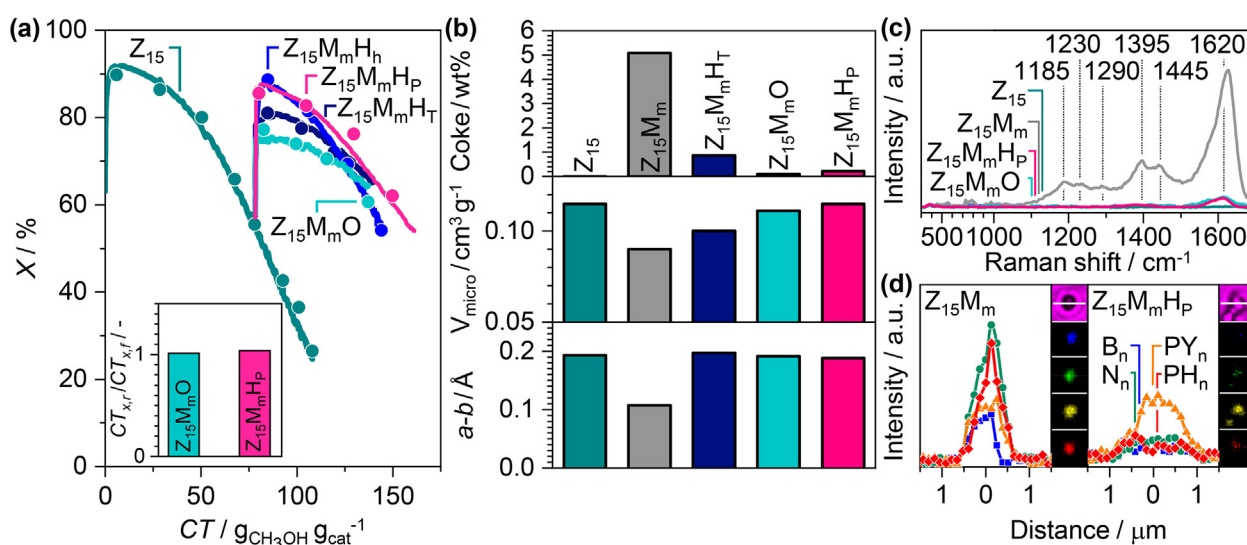
Fig. 6. (a) MTH deactivation profiles, corresponding $CT_{X,r}/CT_{X,f}$ value (inset), (b) coke content, micropore volume, difference of *a* and *b* lattice parameters, (c) Raman spectra, and (d) confocal fluorescence microspectroscopy profiles of $Z_{15}M_mH_P$ catalyst. Markers and lines in (a) indicate conversion calculated from GC-FID and MS analysis, respectively. The MTH performances and corresponding characterization results of other representative Z_{15}-based catalysts are shown for comparison. The Raman spectra in (c) are normalized with respect to the most prominent zeolite peak (*ca.* 381 cm^{-1}). The signal profiles in (d) are derived along the lines indicated in confocal fluorescence micrographs, which are presented on the right of the respective panels. Catalyst reactivation with hydrogen used to obtain $Z_{15}M_mH_P$ catalyst was performed at *T* = 823 K, *P* = 30 bar, c_{H_2} = 100 mol%, *WHSV* = 10.5 g_{H_2} g_{cat}^{-1} h^{-1}, and *tos* = 4 h. Conditions applied in MTH reaction and catalyst reactivation with hydrogen or oxygen for other catalyst samples correspond to those specified in the caption of Fig. 1.

tional reactivation with oxygen. An increased level of coke removal is also reflected by a virtually complete recovery of micropore volume and lattice strain (Fig. 6b). The coke fingerprints in the Raman spectra of $Z_{15}M_mH_P$ catalysts (Fig. 6c) and the fluorescence signals associated with methylated arene species over this material (Fig. 6d) were substantially reduced as well [29]. These results indicate that high-pressure hydrogen treatments of aluminum-rich ZSM-5 zeolites, which are of particular relevance for the methanol-to-aromatics and the emerging carbon-dioxide-to-hydrocarbons transformations [3,48], can attain coke-removal efficiency that is similar to that of conventional reactivation via coke combustion. To shed light on the applicability potential of the catalyst reactivation with high-pressure hydrogen feeds, additional test was performed in which $Z_{15}M_m$ catalyst was treated with H_2 at 30 bars and 873 K for 1.5 h using low hydrogen flow, and the evolving species were collected and analyzed by gas chromatography. Consistent with the analysis presented in Fig. 4, methane, ethane, and aromatics (mostly toluene, xylene, and naptahlene) were the main products detected (Fig. 7). These hydrocarbons were produced with selectivity of *ca.* 30% and account for *ca.* 75 ± 5 wt% of the originally present coke. A high fraction of aromatics with virtually absent semi-hydrogenated aromatic products and low content of ethylene and propylene can be rationalized by higher susceptibility to hydrogenation of aliphatic with respect to aromatic C=C bonds [24]. This can also explain high yields of ethane and methane in the outlet feed, as these can be produced through a hydrogenation coupled with cracking of light alkenes. It is worth noting that hydrogenation treatments were performed in the reactors made of stainless steel, as the latter is preferred material for construction of industrial reactors and because this type of reactors was also applied in previous study on the reaction of coke with hydrogen [12]. At elevated pressures (20–30 bar) and temperatures (823–873 K) used for the hydrogenation treatment, the stainless steel walls can catalyze the hydrogenation of alkenes, as shown by examining the ethene hydrogenation activity of the stainless steel reactor under these reaction conditions (Fig. S11). Nonetheless, the hydrogenation activity of Z_{15} catalyst is still higher than that of the stainless steel reactor, indicating that final product composition is primarily defined by the zeolite catalyst (Fig. S11).

Transformation of coke into light alkanes and valuable aromatics along with high-degree of coke removal poses an interesting alternative to conventional coke combustion into carbon dioxide. It is worth noting that the MTH transformation is typically arranged as a consecutive step to the methanol production, which is currently based on hydrogenation of carbon monoxide, with realistic projections to incorporate the hydrogenation of carbon dioxide in the near future [3,49]. These complementary processes are performed at high pressures (>50 bar), which can provide an access to more affordable high-pressure hydrogen feeds required for MTH catalyst reactivation.

4. Conclusions

Reaction of ZSM-5 catalysts deactivated during MTH with high-pressure hydrogen feed enables to decompose a substantial part of the coke deposits, and thus to restore a significant fraction of initial activity and turnover capacity. The treatment is particularly effective for the zeolites with higher aluminum content, wherein it removes up to 96% of coke deposits, both internal and external, ultimately yielding performances comparable to those of the catalysts reactivated *via* coke oxidation. Decomposition of MTH coke with high-pressure hydrogen feed is proposed to proceed via demethylation of PAHs as well as by the decomposition of the polycyclic rings. It results in formation of light gas (methane and ethane) and more complex products such as alkylated benzenes and naphthalenes, which offers a potential for converting the carbonaceous deposits into valuable hydrocarbons.

Declaration of Competing Interest

The authors declare that they have no known competing financial interests or personal relationships that could have appeared to influence the work reported in this paper.
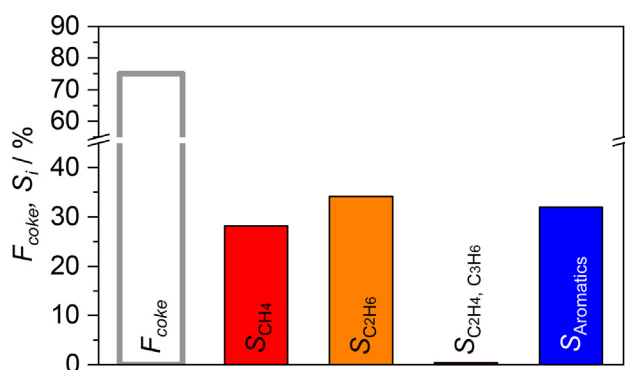
Appendix A. Supplementary material

Selectivities to hydrocarbon products and additional assessments of catalytic activities, X-ray diffractograms, ^{27}Al MAS NMR and ^{27}Al 3Q MAS NMR, FTIR and pyridine adsorption spectra, GC-MS chromatograms, Raman, ^{13}C CP/MAS NMR, and photoemission spectra of the representative catalysts.

Supplementary data to this article can be found online at https://doi.org/10.1016/j.jcat.2022.01.018.

Fig. 7. Fraction of coke transformed into methane, ethane, light alkenes, and aromatics, and corresponding selectivities to these products during hydrogen treatment of $Z_{15}M_m$ catalyst at increased pressure and temperature. Catalyst reactivation with hydrogen was performed at $T = 823$ K, $P = 30$ bar, $c_{H_2} = 100$ mol%, $WHSV = 0.5$ g_{H_2} g_{cat}^{-1} h^{-1}, and $tos = 1.5$ h. Conditions applied in MTH reaction correspond to those specified in the caption of Fig. 1.

References

[1] U. Olsbye, S. Svelle, M. Bjørgen, P. Beato, T.V.W. Janssens, F. Joensen, S. Bordiga, K.P. Lillerud, Conversion of methanol to hydrocarbons: How zeolite cavity and pore size controls product selectivity, Angew. Chem. Int. Ed. 51 (24) (2012) 5810–5831, https://doi.org/10.1002/anie.201103657.

[2] P. Tian, Y. Wei, M. Ye, Z. Liu, Methanol to olefins (MTO): From fundamentals to commercialization, ACS Catal. 5 (3) (2015) 1922–1938, https://doi.org/10.1021/acscatal.5b00007.

[3] I. Yarulina, A.D. Chowdhury, F. Meirer, B.M. Weckhuysen, J. Gascon, Recent trends and fundamental insights in the methanol-to-hydrocarbons process, Nat. Catal. 1 (6) (2018) 398–411, https://doi.org/10.1038/s41929-018-0078-5.

[4] S. Ilias, A. Bhan, Mechanism of the catalytic conversion of methanol to hydrocarbons, ACS Catal. 3 (1) (2013) 18–31, https://doi.org/10.1021/cs3006583.

[5] V. Van Speybroeck, K. De Wispelaere, J. Van der Mynsbrugge, M. Vandichel, K. Hemelsoet, M. Waroquier, First principle chemical kinetics in zeolites: The methanol–to–olefin process as a case study, Chem. Soc. Rev. 43 (21) (2014) 7326–7357, https://doi.org/10.1039/c4cs00146j.

[6] S. Müller, Y. Liu, M. Vishnuvarthan, X. Sun, A.C. Van Veen, G.L. Haller, M. Sanchez-Sanchez, J.A. Lercher, Coke formation and deactivation pathways on H-ZSM-5 in the conversion of methanol to olefins, J. Catal. 325 (2015) 48–59, https://doi.org/10.1016/j.jcat.2015.02.013.

[7] D. Rojo-Gama, M. Signorile, F. Bonino, S. Bordiga, U. Olsbye, K.P. Lillerud, P. Beato, S. Svelle, Structure–deactivation relationships in zeolites during the methanol–to–hydrocarbons reaction: Complementary assessments of the coke content, J. Catal. 351 (2017) 33–48, https://doi.org/10.1016/j.jcat.2017.04.015.

[8] J.E. Schmidt, J.D. Poplawsky, B. Mazumder, Ö. Attila, D. Fu, D.A.M. de Winter, F. Meirer, S.R. Bare, B.M. Weckhuysen, Coke formation in a zeolite crystal during the methanol–to–hydrocarbons reaction as studied with atom probe tomography, Angew. Chem. Int. Ed. 55 (37) (2016) 11173–11177, https://doi.org/10.1002/anie.201606099.

[9] S. Lee, M. Choi, Unveiling coke formation mechanism in MFI zeolites during methanol–to–hydrocarbons conversion, J. Catal. 375 (2019) 183–192, https://doi.org/10.1016/j.jcat.2019.05.030.

[10] T. Liang, J. Chen, Z. Qin, J. Li, P. Wang, S. Wang, G. Wang, M. Dong, W. Fan, J. Wang, Conversion of methanol to olefins over H-ZSM-5 zeolite: Reaction pathway is related to the framework aluminum siting, ACS Catal. 6 (11) (2016) 7311–7325, https://doi.org/10.1021/acscatal.6b01771.0.1021/acscatal.6b01771.s001.

[11] S.S. Arora, D.L.S. Nieskens, A. Malek, A. Bhan, Lifetime improvement in methanol–to–olefins catalysis over chabazite materials by high-pressure H₂ co-feeds, Nat. Catal. 1 (9) (2018) 666–672, https://doi.org/10.1038/s41929-018-0125-2.

[12] X. Zhao, J. Li, P. Tian, L. Wang, X. Li, S. Lin, X. Guo, Z. Liu, Achieving a superlong lifetime in the zeolite-catalyzed MTO reaction under high pressure: Synergistic effect of hydrogen and water, ACS Catal. 9 (4) (2019) 3017–3025, https://doi.org/10.1021/acscatal.8b04402.0.1021/acscatal.8b04402.s001.

[13] M. Choi, K. Na, J. Kim, Y. Sakamoto, O. Terasaki, R. Ryoo, Stable single-unit-cell nanosheets of zeolite MFI as active and long-lived catalysts, Nature. 461 (7261) (2009) 246–249, https://doi.org/10.1038/nature08288.

[14] M. Milina, S. Mitchell, P. Crivelli, D. Cooke, J. Pérez-Ramírez, Mesopore quality determines the lifetime of hierarchically structured zeolite catalysts, Nat. Commun. 5 (2014) 3922, https://doi.org/10.1038/ncomms4922.

[15] R. Feng, X. Yan, X. Hu, Y. Zhang, J. Wu, Z. Yan, Phosphorus-modified b-axis oriented hierarchical ZSM-5 zeolites for enhancing catalytic performance in a methanol to propylene reaction, Appl. Catal. A 594 (2020) 117464, https://doi.org/10.1016/j.apcata.2020.117464.

[16] I. Yarulina, K. De Wispelaere, S. Bailleul, J. Goetze, M. Radersma, E. Abou-Hamad, I. Vollmer, M. Goesten, B. Mezari, E.J.M. Hensen, J.S. Martínez-Espín, M. Morten, S. Mitchell, J. Perez-Ramirez, U. Olsbye, B.M. Weckhuysen, V. Van Speybroeck, F. Kapteijn, J. Gascon, Structure–performance descriptors and the role of Lewis acidity in the methanol–to–propylene process, Nat. Chem. 10 (8) (2018) 804–812, https://doi.org/10.1038/s41557-018-0081-0.

[17] H. Dai, Y. Shen, T. Yang, C. Lee, D. Fu, A. Agarwal, T.T. Le, M. Tsapatsis, J.C. Palmer, B.M. Weckhuysen, P.J. Dauenhauer, X. Zou, J.D. Rimer, Finned zeolite catalysts, Nat. Mater. 19 (10) (2020) 1074–1080, https://doi.org/10.1038/s41563-020-0753-1.

[18] A. Hwang, A. Bhan, Bifunctional strategy coupling Y₂O₃-catalyzed alkanal decomposition with methanol-to-olefins catalysis for enhanced lifetime, ACS Catal. 7 (7) (2017) 4417–4422, https://doi.org/10.1021/acscatal.7b0089410.1021/acscatal.7b00894.s001.

[19] R.G. Copperthwaite, G.J. Hutchings, P. Johnston, S.W. Orchard, Regeneration of pentasil zeolite catalysts using ozone and oxygen, J. Chem. Soc. Faraday Trans. 82 (1986) 1007–1017, https://doi.org/10.1039/F19868201007.

[20] J. Zhou, J. Zhao, J. Zhang, T. Zhang, M. Ye, Z. Liu, Regeneration of catalysts deactivated by coke deposition: A review, Chinese J. Catal. 41 (7) (2020) 1048–1061, https://doi.org/10.1016/S1872-2067(20)63552-5.

[21] K. Barbera, S. Sorensen, S. Bordiga, J. Skibsted, H. Fordsmand, P. Beato, T.V.W. Janssens, Role of internal coke for deactivation of ZSM-5 catalysts after low temperature removal of coke with NO₂, Catal, Sci. Technol. 2 (2012) 1196–1206, https://doi.org/10.1039/c2cy00529h.

[22] D.H. Olson, G. Paul, R. Hill, N. J, F.A. Huggett, US Patent 4,358,395.

[23] F. Bauer, H. Ernst, E. Geidel, R. Schödel, Reactivation of coked H-ZSM-5 by treatment with hydrogen and alkanes, J. Catal. 164 (1) (1996) 146–151, https://doi.org/10.1006/jcat.1996.0370.

[24] S.S. Arora, A. Bhan, Kinetics of aromatics hydrogenation on HBEA, J. Catal. 383 (2020) 24–32, https://doi.org/10.1016/j.jcat.2019.12.039.

[25] B. Chan, L. Radom, Zeolite-catalyzed hydrogenation of carbon dioxide and ethene, J. Am. Chem. Soc. 130 (30) (2008) 9790–9799, https://doi.org/10.1021/ja800840q.

[26] J. Kanai, J.A. Martens, P.A. Jacobs, On the nature of the active sites for ethylene hydrogenation in metal-free zeolites, J. Catal. 133 (1992) 527–543, https://doi.org/10.1016/0021-9517(92)90259-K.

[27] A.A. Coelho, TOPAS and TOPAS-Academic: An optimization program integrating computer algebra and crystallographic objects written in C++, J. Appl. Crystallogr. 51 (2018) 210–218, https://doi.org/10.1107/S1600576718000183.

[28] C.A. Emeis, Determination of integrated molar extinction coefficients for infrared absorption bands of pyridine adsorbed on solid acid catalysts, J. Catal. 141 (1993) 347–354, https://doi.org/10.1006/jcat.1993.1145.

[29] M. Gao, H. Li, W. Liu, Z. Xu, S. Peng, M. Yang, M. Ye, Z. Liu, Imaging spatiotemporal evolution of molecules and active sites in zeolite catalyst during methanol-to-olefins reaction, Nat. Commun. 11 (2020) 3641, https://doi.org/10.1038/s41467-020-17355-6.

[30] J. Schindelin, I. Arganda-Carreras, E. Frise, V. Kaynig, M. Longair, T. Pietzsch, S. Preibisch, C. Rueden, S. Saalfeld, B. Schmid, J.-Y. Tinevez, D.J. White, V. Hartenstein, K. Eliceiri, P. Tomancak, A. Cardona, Fiji: An open-source platform for biological-image analysis, Nat. Methods. 9 (7) (2012) 676–682, https://doi.org/10.1038/nmeth.2019.

[31] F. Orlando, A. Waldner, T. Bartels-Rausch, M. Birrer, S. Kato, M.-T. Lee, C. Proff, T. Huthwelker, A. Kleibert, J. van Bokhoven, M. Ammann, The environmental photochemistry of oxide surfaces and the nature of frozen salt solutions: A new in situ XPS approach, Top. Catal. 59 (5-7) (2016) 591–604, https://doi.org/10.1007/s11244-015-0515-5.

[32] K. Roy, L. Artiglia, J.A. van Bokhoven, Ambient pressure photoelectron spectroscopy: Opportunities in catalysis from solids to liquids and introducing time resolution, ChemCatChem. 10 (4) (2018) 666–682, https://doi.org/10.1002/cctc.201701522.

[33] C.J. Powell, A. Jablonski, NIST electron inelastic-mean-free-path database, 2000.

[34] J. Kim, M. Choi, R. Ryoo, Effect of mesoporosity against the deactivation of MFI zeolite catalyst during the methanol-to-hydrocarbon conversion process, J. Catal. 269 (1) (2010) 219–228, https://doi.org/10.1016/j.jcat.2009.11.009.

[35] R. Gounder, E. Iglesia, Catalytic hydrogenation of alkenes on acidic zeolites: Mechanistic connections to monomolecular alkane dehydrogenation reactions, J. Catal. 277 (1) (2011) 36–45, https://doi.org/10.1016/j.jcat.2010.10.013.

[36] D. Rojo-Gama, M. Nielsen, D.S. Wragg, M. Dyballa, J. Holzinger, H. Falsig, L.F. Lundegaard, P. Beato, R.Y. Brogaard, K.P. Lillerud, U. Olsbye, S. Svelle, A straightforward descriptor for the deactivation of zeolite catalyst H-ZSM-5, ACS Catal. 7 (12) (2017) 8235–8246, https://doi.org/10.1021/acscatal.7b0219310.1021/acscatal.7b02193.s001.

[37] S.M. Campbell, D.M. Bibby, J.M. Coddington, R.F. Howe, Dealumination of HZSM-5 zeolites, J. Catal. 161 (1) (1996) 350–358, https://doi.org/10.1006/jcat.1996.0192.

[38] R.H. Meinhold, D.M. Bibby, ²⁷Al and ²⁹Si n.m.r. studies of HZSM-5: Part 2. The effect of coke formation, Zeolites. 10 (3) (1990) 146–150, https://doi.org/10.1016/0144-2449(90)90037-R.

[39] S.M.T. Almutairi, B. Mezari, E.A. Pidko, P.C.M.M. Magusin, E.J.M. Hensen, Influence of steaming on the acidity and the methanol conversion reaction of HZSM-5 zeolite, J. Catal. 307 (2013) 194–203, https://doi.org/10.1016/j.jcat.2013.07.021.

[40] A.J. Jones, R.T. Carr, S.I. Zones, E. Iglesia, Acid strength and solvation in catalysis by MFI zeolites and effects of the identity, concentration and location of framework heteroatoms, J. Catal. 312 (2014) 58–68, https://doi.org/10.1016/j.jcat.2014.01.007.

[41] M. Signorile, D. Rojo-Gama, F. Bonino, P. Beato, S. Svelle, S. Bordiga, Topology–dependent hydrocarbon transformations in the methanol-to-hydrocarbons reaction studied by: Operando UV-Raman spectroscopy, Phys. Chem. Chem. Phys. 20 (41) (2018) 26580–26590, https://doi.org/10.1039/c8cp04240c.

[42] Y.T. Chua, P.C. Stair, An ultraviolet Raman spectroscopic study of coke formation in methanol to hydrocarbons conversion over zeolite H-MFI, J. Catal. 213 (1) (2003) 39–46, https://doi.org/10.1016/S0021-9517(02)00026-X.

[43] H. An, F. Zhang, Z. Guan, X. Liu, F. Fan, C. Li, Investigating the coke formation mechanism of H-ZSM-5 during methanol dehydration using operando UV-Raman spectroscopy, ACS Catal. 8 (10) (2018) 9207–9215, https://doi.org/10.1021/acscatal.8b0092810.1021/acscatal.8b00928.s001.

[44] F. Bauer, W.H. Chen, Q. Zhao, A. Freyer, S. Bin Liu, Improvement of coke-induced selectivity of H-ZSM-5 during xylene isomerization, Micropor. Mesopor. Mater. 47 (2001) 67–77, https://doi.org/10.1016/S1387-1811(01)00318-3.

[45] Q. Qian, J. Ruiz-Martínez, M. Mokhtar, A.M. Asiri, S.A. Al-Thabaiti, S.N. Basahel, B.M. Weckhuysen, Single-particle spectroscopy of alcohol-to-olefins over SAPO-34 at different reaction stages: Crystal accessibility and hydrocarbons reactivity, ChemCatChem 6 (3) (2014) 772–783, https://doi.org/10.1002/cctc.201300962.

[46] A.N. Mlinar, P.M. Zimmerman, F.E. Celik, M. Head-Gordon, A.T. Bell, Effects of Brønsted-acid site proximity on the oligomerization of propene in H-MFI, J. Catal. 288 (2012) 65–73, https://doi.org/10.1016/j.jcat.2012.01.002.

[47] S.J. Jong, A.R. Pradhan, J.F. Wu, T.C. Tsai, S. Bin Liu, On the regeneration of coked H-ZSM–5 catalysts, J. Catal. 174 (1998) 210–218, https://doi.org/10.1006/jcat.1998.1971.

[48] A. Dokania, A. Dutta Chowdhury, A. Ramirez, S. Telalovic, E. Abou-Hamad, L. Gevers, J. Ruiz-Martinez, J. Gascon, Acidity modification of ZSM-5 for enhanced production of light olefins from CO₂, J. Catal. 381 (2020) 347–354, https://doi.org/10.1016/j.jcat.2019.11.015.

[49] J. Zhong, X. Yang, Z. Wu, B. Liang, Y. Huang, T. Zhang, State of the art and perspectives in heterogeneous catalysis of CO₂ hydrogenation to methanol, Chem. Soc. Rev. 49 (5) (2020) 1385–1413, https://doi.org/10.1039/c9cs00614a.